



저작자표시-동일조건변경허락 2.0 대한민국

이용자는 아래의 조건을 따르는 경우에 한하여 자유롭게

- 이 저작물을 복제, 배포, 전송, 전시, 공연 및 방송할 수 있습니다.
- 이차적 저작물을 작성할 수 있습니다.
- 이 저작물을 영리 목적으로 이용할 수 있습니다.

다음과 같은 조건을 따라야 합니다:



저작자표시. 귀하는 원저작자를 표시하여야 합니다.



동일조건변경허락. 귀하가 이 저작물을 개작, 변형 또는 가공했을 경우에는, 이 저작물과 동일한 이용허락조건하에서만 배포할 수 있습니다.

- 귀하는, 이 저작물의 재이용이나 배포의 경우, 이 저작물에 적용된 이용허락조건을 명확하게 나타내어야 합니다.
- 저작권자로부터 별도의 허가를 받으면 이러한 조건들은 적용되지 않습니다.

저작권법에 따른 이용자의 권리는 위의 내용에 의하여 영향을 받지 않습니다.

이것은 [이용허락규약\(Legal Code\)](#)을 이해하기 쉽게 요약한 것입니다.

[Disclaimer](#)

Dissertation of the degree of Doctor of Philosophy

**A Population-Based Tissue Probability
Map-Driven Level Set Method for Fully
Automated Mammographic Density
Estimations**

유방 밀도 자동 측정을 위한 통계적 조직
확률 모델 기반의 Level Set 방법

2014 년 8 월

서울대학교 대학원
협동과정 방사선응용생명과학 전공

김 영 우

**A Population-Based Tissue
Probability Map-Driven Level Set
Method for Fully Automated
Mammographic Density Estimations**

by

Youngwoo Kim

A thesis submitted to the Interdisciplinary Program in partial fulfillment of the requirements for the Degree of Doctor of Philosophy in Radiation Applied Life Science at Seoul National University College of Medicine

July 2014

Approved by Thesis Committee:

Chairman	Kwang Suk Park	_____
Vice Chairman	Jong Hyo Kim	_____
Member	Woo Kyung Moon	_____
Member	Jae Sung Lee	_____
Member	Byung Woo Hong	_____

ABSTRACT

A Population-Based Tissue Probability Map-Driven Level Set Method for Fully Automated Mammographic Density Estimations

Youngwoo Kim

Interdisciplinary Program of Radiation Applied Life Science
Seoul National University College of Medicine

Introduction: A major challenge when distinguishing glandular tissues on mammograms, especially for area-based estimations, lies in determining a boundary on a hazy transition zone from adipose to glandular tissues. This stems from the nature of mammography, which is a projection of superimposed tissues consisting of different structures. In this paper, I present a novel segmentation scheme which incorporates the learned prior knowledge of experts into a level set framework for fully automated mammographic density estimations.

Methods: I modeled the learned knowledge as a population-based tissue probability map (PTPM) that was designed to capture the classification of experts' visual systems. The PTPM was constructed using an image database of a selected population consisting of 397 cases. Three mammogram experts

extracted regions for dense and fatty tissues on digital mammograms, which was an independent subset used to create a tissue probability map for each ROI based on its local statistics. This tissue class probability was taken as a prior in the Bayesian formulation and was incorporated into a level set framework as an additional term to control the evolution and followed the energy surface designed to reflect experts' knowledge as well as the regional statistics inside and outside of the evolving contour.

Results: A subset of 100 digital mammograms, which was not used in constructing the PTPM, was used to validate the performance. The energy was minimized when the initial contour reached the boundary of the dense and fatty tissues, as defined by experts. The correlation coefficient between mammographic density measurements made by experts and measurements by the proposed method was 0.93, while that with the conventional level set was 0.47.

Conclusions: The proposed method showed a marked improvement over the conventional level set method in terms of accuracy and reliability. This result suggests that the proposed method successfully incorporated the learned knowledge of the experts' visual systems and has the potential to be used as an automated and quantitative tool for estimations of mammographic breast density levels.

Keywords: prior statistics, level set, mammographic breast density, quantitative measure, full field digital mammography

Student number: 2010-30598

CONTENTS

Abstract	i
Contents.....	iii
List of figures	v
List of tables	viii
1. INTRODUCTION	1
2. THEORY	4
2.1. Conventional Region-Based Level Set Segmentation.....	5
2.2. PTPM-Driven Level Set Segmentation.....	7
3. MATERIALS AND METHODS	10
3.1. Database	10
3.2. Experts' Measurement of the Mammographic Percent Density.....	11
3.3. System Overview	12
3.4. Preprocessing.....	13
3.5. PTPM Construction.....	17
3.6. Density Estimation	23
4. RESULTS	27
4.1. Visual Assessment of Contours	27
4.2. Agreement with the Experts' Assessments	27
4.3. Evaluation on Various ROI Scales	32
4.4. Effect of the Proposed Procedures	32
5. DISCUSSION	35

6. CONCLUSIONS	42
REFERENCES	43
Abstract in Korean	47
Acknowledgement	49

LIST OF FIGURES

Figure. 1. Illustration of signed distance function. Red circle in (a) is a given contour represented by a zero level set of the signed distance function which is visualized in (b) where the zero level set is illustrated as black hyperplane	4
Figure. 2. A schematic diagram of the overall system	12
Figure. 3. A typical histogram of the digital mammograms used in this study. The annotations denote the means for the background region, the background, and the breast area	13
Figure. 4. Examples of histogram within the breast area in a mammogram: (a) before intensity range alignment, (b) after intensity range alignment. The staple-shaped red solid lines on the top of each histogram represent the intensity range of the fatty region, whereas the red arrows indicate the offset intensity. The range of the fatty region in each mammogram was that determined by the experts using an interactive thresholding	15
Figure. 5. A 2D scatter plot of the mean and standard deviation of ROIs within fatty and dense regions: (a) before the histogram shift, (b) after the histogram shift	16
Figure. 6. ROI selection in the breast area: (a) a preprocessed mammogram in which the boundaries of the breast area and dense regions are shown in a color overlay with yellow and red, and (b) the selected ROIs within dense and fatty regions marked as red and green circles.	18
Figure. 7. Scatter plot of the obtained statistical features from 297	

mammograms (red: dense region, green: fatty region).	19
Figure. 8. The calculated probability density function of (a) dense region and (b) fatty region by using non-parametric estimation scheme.....	21
Figure. 9. The PTPM obtained from the population of the dense region derived from the nonparametric probability density function.	22
Figure. 10. A pictorial example of the prior probability estimation result of a given mammogram: (a) the input mammogram, and (b)–(c) the probability of each pixel being a dense region and a fatty region, respectively. Note that the color saturation level represents the probability value.....	23
Figure. 11. The evolution of contours at (a) 0, (b) 5, (c) 10, (d) 30, and (f) final iterations, respectively.....	24
Figure. 12. A comparison of the estimations between (top) the results of the interactive thresholding with the in-house software and (bottom) the outputs of the proposed method. The boundaries of the breast areas are denoted by the yellow solid line while those of the dense regions are depicted with the red solid line.....	25
Figure. 13. 2D scatter plots of the experts' estimation versus the automated estimation process using (a, b, and c) the proposed method against the experts' assessments, and (d) the CV level set method. The horizontal and vertical axes are MPD calculated by the automated methods and by the experts, respectively. The correlation coefficients are shown near the trend lines. Note that the result of the proposed method in (a) was trained with the entire training dataset, whereas the results in (b) and (c) were trained with the first and second training	

subsets.	26
Figure. 14. Bland-Altman plot of the experts' assessments against the (a) proposed and (b) conventional methods. The horizontal and vertical axes are the mean of two estimations and difference between the experts' and automated estimation, respectively.	28
Figure. 15. Example mammograms with a hazy transition of the pixel intensities from fatty to dense regions, where the estimated mammographic percent density is shown on the top of each segmentation result: (a) the reference estimate from the radiologists, and estimates with (b) the CV method and (c) the proposed method. Note that the deviations from the reference estimates are shown in parentheses below the percent density.	29
Figure. 16. A 2D scatter plot of estimation results by the proposed method trained with D_{T1} versus D_{T2}	30
Figure. 17. 2D scatter plots of the experts' estimation versus the automated estimation process using ROI size of (a) 4mm, (b) 6mm, (c) 12mm, (d) 15mm, (e) 20mm, and (f) 30mm.	34
Figure. 18. The performance graph with respect to various ROI sizes. The dashed line indicates the performance of the proposed method with ROI size utilized in this study (10mm).	36
Figure. 19. The effect of the proposed order of procedures in this study.	37
Figure. 20. An example case where the estimation result of proposed method disagreed with that of experts: (a) original mammogram with automated extraction of breast region, (b) result of experts' interactive thresholding, (c) automated estimation result of the proposed method.	38

LIST OF TABLES

TABLE I. Patient information with respect to the BI-RADS category10

TABLE II. A comparison of the results between the radiologists’
interactive estimation results using the in-house software and the
outputs of the proposed method31

1. INTRODUCTION

Mammographic breast density is becoming a central subject of studies in diverse areas of breast cancer research. Mammographic breast density basically refers to the proportion of the radiographically dense region within the breast area, reflecting the relative amount of glandular tissues within the breast, which is known to be associated with many biological events in the development of breast cancer, reactions to treatment, and recurrence [1-6]. Since the pioneering reports by Wolfe [7], there has been a profusion of studies indicating that a higher breast density level means a greater risk of breast cancer for women [1-3]. Furthermore, accumulated studies suggest that the mammographic density can be used as an effective biomarker across all stages of patient care for those with breast cancer, including the screening of breast cancer as a risk-prediction factor [1-3], decisions on appropriate treatments (i.e., chemotherapy, hormone replacement therapy, and radiotherapy) [6, 8], monitoring of the treatment [4], and the recurrence prediction of breast cancer [5].

Despite its growing importance, the manner in which breast density is measured remains crude and subjective in clinical practice. Radiologists report mammographic densities based on their visual judgments according to the Breast Imaging Reporting and Data System (BI-RADS) classification protocol [9]. This protocol requires radiologists to assign mammograms into one of four categories (i.e., I, II, III, and IV) according to the proportion of the dense region with a 25% interval based on the visual judgment. While this

qualitative measure has been used in studies of breast cancer risk models for extremely fatty and dense breasts, several studies have also reported its considerable intra- and inter-rater variability [10, 11]. Over the past few decades, numerous approaches have been proposed for objective estimations of the mammographic density to overcome the aforementioned limitations. The pioneering work by Byng *et al.* provide, for the first time, the mammographic percent density software using an interactive thresholding technique, which has become the most widely used and validated means of studying the association between the mammographic percent density and breast cancer risk [12-14]. Nevertheless, this technique is also time-consuming and associated with rater dependency, as it requires the user to select two thresholds based on a visual judgment [15]. These limitations have led to efforts creating fully automated techniques for mammographic breast density estimations to be more objective and reproducible.

In the literature, estimation methods can be classified into three categories: histogram-based [16-18], texture analysis [19-26], and imaging physics-based methods [27-33]. Histogram-based methods use the characteristics of a gray-level histogram, such as its statistical features (e.g., standard deviation and skewness), as a function of the distance from the skin [16] and the shape of the histogram [17, 18]. Another group of studies make use of texture properties to estimate the mammographic breast density. Fuzzy connectedness, K-means, fuzzy c-means (FCM) clustering algorithms, and statistical discrepancies are utilized in several studies [19-24], and the integration of features including the location, intensity, texture, and global

context is utilized in another [26]. There have also been approaches which employ the image acquisition parameters of mammograms (i.e., tube voltage (kVp), anode material, filtration, and compressed breast thickness) [27-30]. These approaches utilize standardization or calibration techniques for breast density measurements in film-screen mammograms [30, 32] and full-field digital mammography (FFDM) [27-29, 34]. Furthermore, Heine *et al.* have studied an X-ray attenuation measurement technique [33, 35] with applications to breast density estimation and BI-RADS categorization with the calibrated mammograms by using population-based parameters [36, 37].

In this paper, I introduce a novel segmentation method which incorporates learned knowledge from experts into a level set framework [38-40] to effectively segment dense tissue out of the surrounding fatty tissue. The learned knowledge is captured in the form of a population-based tissue probability map (PTPM), which is taken as prior probability in the Bayesian formulation and is incorporated into a level set framework as an additional term to control the evolution and follow the energy surface, which is newly designed to reflect the prior tissue probability as well as the regional statistics inside and outside of the evolving contour.

Throughout this paper, I use the term dense region to indicate an area which corresponds to radio-dense tissues, including glandular, fibrous, and epithelial tissues, whereas fatty region refers to an area reflecting radiolucent adipose tissue on mammograms.

2. THEORY

In this section, I state the level set segmentation problem from the perspective of Bayesian inference and describe how learned knowledge can be used to derive a novel level set technique.

$$p(\phi|f) = \frac{p(f|\phi)p(\phi)}{p(f)} \quad (1)$$

The segmentation problem can be conceived of as the act of finding a solution of the Bayesian formula in (1) which maximizes the conditional (posterior) probability if an image f is given; in other words, the conditional probability is maximized if the segmentation contour is located at the desired boundary between the two objects to be separated.

In (1), the signed distance function $\phi(\mathbf{x};t):\Omega \rightarrow \mathbb{R}$ is a monotonically increasing or decreasing function satisfying the *Lipschitz* continuity, in which a contour $\partial\omega$ in Ω is represented by the zero level set

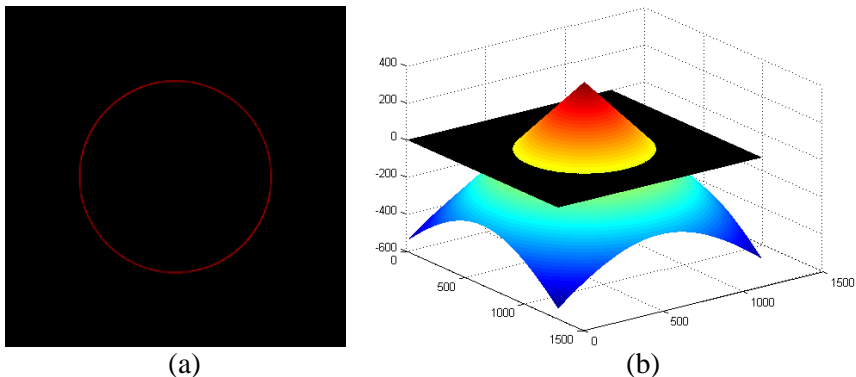


Figure 1. Illustration of signed distance function. Red circle in (a) is a given contour represented by a zero level set of the signed distance function which is visualized in (b) where the zero level set is illustrated as black hyperplane.

$\phi(\mathbf{x};t)=0$. Here, ω is a set of pixels satisfying $\phi(\mathbf{x};t)>0$; $\mathbf{x}=(x,y)$ is the pixel location, in which x and y are the horizontal and vertical pixel position, respectively; and t is a time parameter. The illustration of the signed distance function is shown in Fig. 1.

2.1. Conventional Region-Based Level Set Segmentation

In this subsection, I revisit the Chan-Vese (CV) level set model from the perspective of Bayesian inference. In the CV model [41], the energy functional was defined such that the sum of the variances of two objects is minimized when the evolving closed curve C suitably partitions the two objects succeeding the piecewise-constant Mumford-Shah functional. Due to the piecewise-constant assumption in the CV model, the prior probabilities of the two regions can be set to be equal (i.e., $p(\phi)=0.5$), where the likelihood is defined as follows:

$$p(f|\phi) = e^{-\int_{\omega} (f(\mathbf{x})-c_{in})^2 d\mathbf{x}} \times e^{-\int_{\Omega\setminus\omega} (f(\mathbf{x})-c_{out})^2 d\mathbf{x}} \times e^{-\int_{\partial\omega} s ds} \quad (2)$$

Here, s is a parameterization variable of $\partial\omega$ and c_{in} and c_{out} are the mean intensity values inside and outside of $\partial\omega$, respectively. With the likelihood and prior probability defined as shown above, it is possible to obtain the optimal value of ϕ which maximizes the conditional probability

in (1), which is equivalent to minimizing the negative log-likelihood. This results in the following functional:

$$\begin{aligned}
E_{image}(\phi(\mathbf{x}), c_{in}, c_{out}) &= \int_{\Omega} |\nabla H(\phi(\mathbf{x}))| d\mathbf{x} \\
&+ \int_{\Omega} (f(\mathbf{x}) - c_{in})^2 H(\phi(\mathbf{x})) d\mathbf{x} \\
&+ \int_{\Omega} (f(\mathbf{x}) - c_{out})^2 (1 - H(\phi(\mathbf{x}))) d\mathbf{x}
\end{aligned} \tag{3}$$

$$c_{in} = \frac{\int_{\Omega} f(\mathbf{x}) H(\phi(\mathbf{x})) d\mathbf{x}}{\int_{\Omega} H(\phi(\mathbf{x})) d\mathbf{x}} \tag{4}$$

$$c_{out} = \frac{\int_{\Omega} f(\mathbf{x}) (1 - H(\phi(\mathbf{x}))) d\mathbf{x}}{\int_{\Omega} (1 - H(\phi(\mathbf{x}))) d\mathbf{x}}. \tag{5}$$

In (3)–(5), $H(\cdot)$ is the Heaviside function that indicates the inside of the contour which was used for unifying the complementary domains (i.e., ω , $\Omega \setminus \omega$, and $\partial\omega$) into the single domain (i.e., Ω); it was approximated as a smooth function $H_{\varepsilon} = \frac{1}{2} \left[1 + \frac{2}{\pi} \arctan\left(\frac{x}{\varepsilon}\right) \right]$ so that the energy functional can be differentiable. The first term in (3) maintains the minimal length of the separating boundary, whereas the last two terms ensure that the intensity variance is minimized. During the curve propagation process, edge information was not used at all, as it is sensitive to noise. The energy functional in (3) was eventually minimized using a partial differential equation (PDE) with respect to ϕ , resulting in the following the motion

equation:

$$\begin{aligned} \frac{\partial \phi}{\partial t} &= -\frac{\partial E_{image}}{\partial \phi} \\ &= \delta(\phi) \left[\operatorname{div} \left(\frac{\nabla \phi}{|\nabla \phi|} \right) - (f - c_{in})^2 + (f - c_{out})^2 \right] \quad (6) \end{aligned}$$

Here, $\delta(\cdot)$ is the delta function, which served to detect the spatial position of the image.

2.2. PTPM-Driven Level Set Segmentation

Here, I describe how the learned knowledge is modeled and incorporated into the level set framework to derive its energy functional and motion equation. I modeled the learned knowledge as a prior probability in a Bayesian formula. During the training process, an expert was given an image database of a selected population, attaining knowledge associating local statistics on mammograms of tissue types in the breast. I captured this knowledge from experts in the form of a PTPM, which provided prior probability of tissue types when the local statistics are given at a pixel. Details of the PTPM construction process are described in section 3.5..

Contrary to the CV model, in which the prior probability had a constant value of 0.5, I formulated the prior probability to make use of the PTPM, as follows:

$$p(\phi|P_+, P_-) = \frac{\int_{\omega} P_+(\mathbf{x}) d\mathbf{x}}{\int_{\omega} d\mathbf{x}} \times \frac{\int_{\Omega \setminus \omega} P_-(\mathbf{x}) d\mathbf{x}}{\int_{\Omega \setminus \omega} d\mathbf{x}} \quad (7)$$

Here, $P_+(\mathbf{x})$ and $P_-(\mathbf{x})$ are the class probabilities of the regions inside ($\phi > 0$) and outside ($\phi < 0$) of the contour $\partial\omega$, respectively. Note that in (7), the prior probability $p(\phi|P_+, P_-)$ given P_+ and P_- is maximized if the class probabilities of each region are maximized. With the prior probability of (7) inserted into (1), a new energy functional was derived as the sum of two energies, each representing the energy directly related to the given image and the prior probability, as in (8).

$$\begin{aligned} \hat{\phi} &= \arg \max p(\phi|f, P_+, P_-) \\ &\propto \arg \max \left[p(f|\phi) p(\phi|P_+, P_-) \right] \\ &= \arg \min \left[-\ln(p(f|\phi)) - \ln(p(\phi|P_+, P_-)) \right] \\ &= \arg \min (E_{image} + E_{prior}). \end{aligned} \quad (8)$$

Applying the Heaviside function to (7) gives

$$\begin{aligned} E_{prior}(\phi(\mathbf{x})) &= -\int_{\Omega} \ln P_+(\mathbf{x}) H(\phi(\mathbf{x})) d\mathbf{x} \\ &\quad - \int_{\Omega} \ln P_-(\mathbf{x}) (1 - H(\phi(\mathbf{x}))) d\mathbf{x}. \end{aligned} \quad (9)$$

I adopted the same energy functional for E_{image} as used in the CV model. The total energy was given as

$$E(\phi(\mathbf{x}), c_{in}, c_{out}) = E_{image}(\phi(\mathbf{x}), c_{in}, c_{out}) + E_{prior}(\phi(\mathbf{x})). \quad (10)$$

The final step was to obtain the motion equation to evolve the contour regarding the time parameter t to gradually minimize the functional $E(\phi, c_{in}, c_{out})$ with respect to ϕ ; thus, I solved the associated Euler-Lagrange equation [42] in (11) and obtain the motion equation in (12).

$$\frac{\partial E(\phi(\mathbf{x}), c_{in}, c_{out})}{\partial \phi(\mathbf{x})} = -\frac{\partial \phi(\mathbf{x})}{\partial t} \quad (11)$$

$$\begin{aligned} \frac{\partial \phi(\mathbf{x})}{\partial t} = \delta(\phi(\mathbf{x})) & \left[\operatorname{div} \left(\frac{\nabla \phi(\mathbf{x})}{|\nabla \phi(\mathbf{x})|} \right) - (f(\mathbf{x}) - c_{in})^2 \right. \\ & \left. + (f(\mathbf{x}) - c_{out})^2 + \ln \frac{P_+(\mathbf{x})}{P_-(\mathbf{x})} \right] \end{aligned} \quad (12)$$

3. MATERIALS AND METHODS

3.1. Database

This study received institutional review board (IRB) approval from Seoul National University Hospital for the study of fully automated mammographic density estimation and its association with breast cancer for 412 patients from the breast cancer screening center of the same institute. As a part of this study, 397 anonymized craniocaudal (CC) view full-field digital mammograms from 349 female patients [mean age, 50.5 yr \pm 10.3 (SD); range, 27–78 yr] were selected, in which 63 patients with prior breast cancer surgery or mammograms with any abnormal findings (i.e., micro-calcifications, mass, or implant) were excluded. The exams were taken from January to December of 2008, and were acquired with an FFDM system (Senograph 2000D, GE Healthcare, USA).

The images had a resolution of 100 $\mu\text{m}/\text{pixel}$ and a pixel matrix of 2294×1914 . They were post-processed using Premium View (GE Healthcare) software, which produced adaptive histogram equalized 12-bit gray-level images [43]. Of the 397 mammograms, 100 mammograms from 100 women

TABLE I. Patient information with respect to the BI-RADS category.

BI-RADS Category	No. of MMGs	Mean Age \pm SD	Breast Area \pm SD (cm ²)	Dense Area \pm SD (cm ²)	Density \pm SD (%)
I	24	62.6 \pm 6	1343.5 \pm 469	244.6 \pm 87	18.7 \pm 5
II	144	55.6 \pm 9	963.4 \pm 376	330.3 \pm 131	35.9 \pm 11
III	129	48.3 \pm 9	796.1 \pm 272	387.4 \pm 148	49.5 \pm 11
IV	100	42.8 \pm 8	689.1 \pm 202	458.9 \pm 141	66.8 \pm 10
Total	397	50.5 \pm 10	864.1 \pm 354	375.6 \pm 149	46.9 \pm 17

were randomly selected for validation, and 297 mammograms from 249 women were used as a training set. The woman-based separation of the training and validation set was carried out to avoid potential bias so that mammograms from a single woman appear in either the training or validation set, considering the fact that the left and right breasts of a woman are highly symmetric and show similar characteristics. The patient information, including the mean age, breast area, dense area, and mammographic density, is shown in Table I.

In addition, I divided the training set of 297 mammograms from 249 women D_T into two independent subsets in which the first subset $D_{T_1} \subset D_T$ consisted of 154 mammograms from 125 women and $D_{T_2} = D_T^C$ of 143 mammograms from 124 women. The training set D_T was used for constructing the PTPM of the pooled population, while D_{T_1} and D_{T_2} were used for constructing the PTPM of partial population in order to verify the robustness of the proposed method against the population-dependent training effect.

3.2. Experts' Measurement of the Mammographic Percent Density

In this study, I recruited three experts with more than 10 years of mammogram experience. Two were breast radiologists and one was a breast surgeon. The experts were provided with in-house software and the Cumulus4 software (University of Toronto) [44] for training and validation purpose,

respectively. The in-house software exactly replicated the Cumulus4 in that it utilized the interactive thresholding technique to determine the boundary between dense and fatty regions, but it was different from the Cumulus4 in that it carried out a two-step procedure automatically before presenting an image to the user. Specifically, it separated the breast area from the background using a technique described in section 3.4 and adjusted the window width and level for an improved visualization of the mammogram so that the users can determine the threshold and save the estimation results conveniently. I used the in-house software in PTPM construction phase in section 3.5 only, in which the binary masks generated by the software were taken to mark the dense region of the mammogram, and the experts' estimation results by using Cumulus4 were used for the performance evaluation of the proposed method.

3.3. System Overview

The proposed method was implemented in three steps: preprocessing, PTPM construction, and density estimation. The overall procedure is shown in Fig. 2. In the preprocessing step, the breast area was extracted from an input mammogram, and the intensity range within the breast area was aligned. In

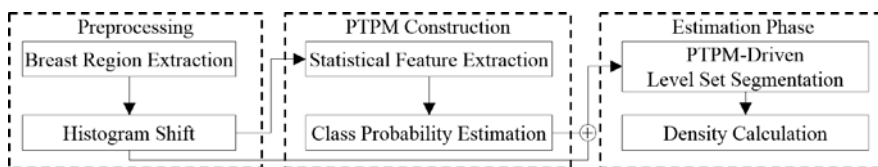


Figure 2. A schematic diagram of the overall system.

the PTPM construction step, statistical features were extracted from the segmented mammograms of the training data set, from which the prior probability map was constructed. In the last step, the PTPM-driven level set was applied to each mammogram to segment the dense region. This step was followed by the calculation of the breast density percentage.

3.4. Preprocessing

The preprocessing began with the down-sampling of an input mammogram by a factor of 2 to reduce the computational time from the resolution of an original image, 2294×1914 , to 1147×957 using *Lanczos* interpolation, after which the breast area was extracted by histogram modeling. The histogram shape of the FFDM used in this study was shown to be bimodal, as depicted

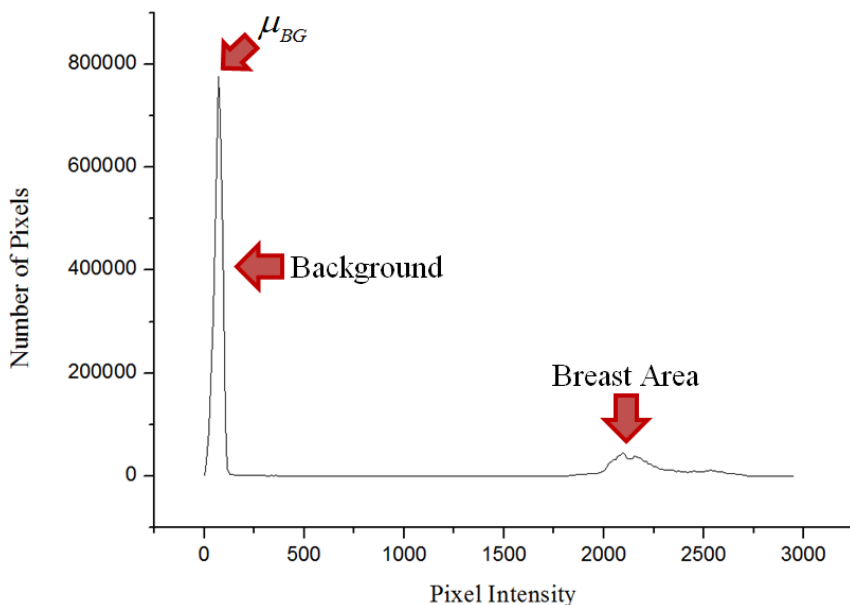


Figure 3. A typical histogram of the digital mammograms used in this study. The annotations denote the means for the background region, the background, and the breast area.

in Fig. 3, in which the first peak corresponds to the background and the second peak reflects the breast area. The first peak is always distinct showing a narrow and higher shape due to the lower intensity variation in the background area. Eying this unique property, I modeled the background peak as a Gaussian distribution in which the mean value μ_{BG} corresponded to the mode value of the entire histogram. Then, its standard deviation σ_{BG} was computed by the root-mean-square (RMS) method, and the threshold of the breast area, t_B , was determined as $\mu_{BG} + K \cdot \sigma_{BG}$, in which K is a constant which was set to 3.0 heuristically.

Once I obtained the breast area, alignment of the intensity range was carried out by means of a histogram shift process. The mammograms of the patient population exhibited diverse intensity distribution patterns arising from differences in the breast thickness, exposure conditions, tube type-filter combinations, and grid types. This diversity of the intensity distribution motivated us to introduce an intermediate processing step to compensate for the intensity range variation before proceeding.

Shown in Fig. 4(a) are the examples of the intensity range of the breast area of FFDM cases with respect to each BI-RADS category. The first step, in the intensity range alignment process, was to determine the offset intensity i_{off} , which can be thought of as the leading edge of the histogram slope of the breast area. Using this leading edge as a reference value, the intensity ranges of the mammograms were aligned to have a consistent distribution over the entire population of mammograms. The determination of

i_{off} and the histogram shift operation were carried out according to (13)–(14), respectively.

$$i_{off} = \arg \min_{i > t_B} (h(i) > M) \quad (13)$$

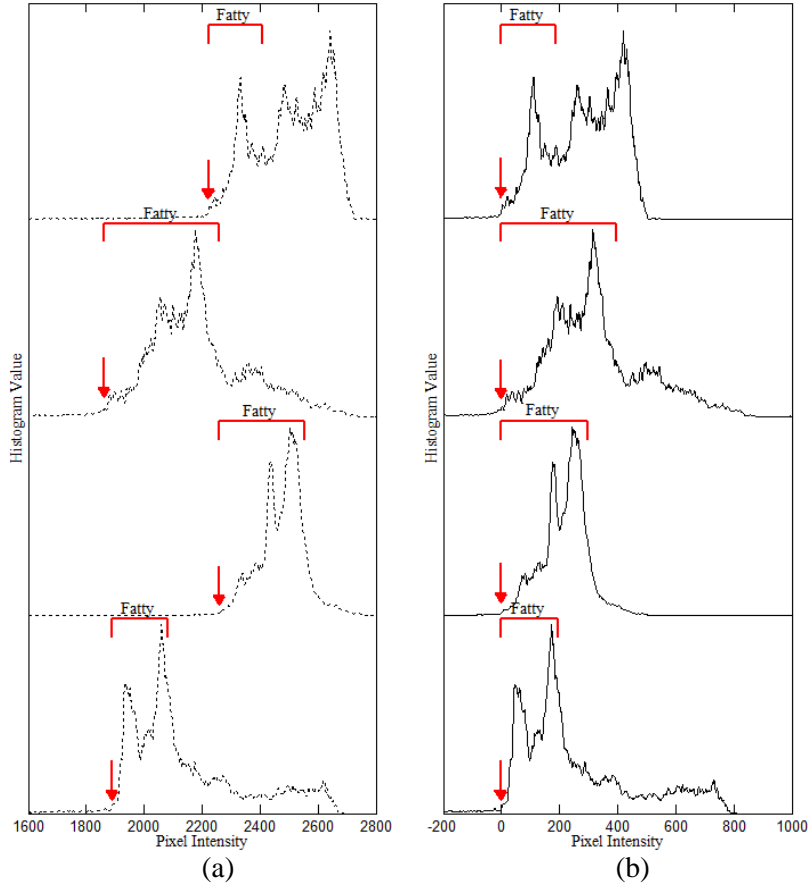


Figure 4. Examples of histogram within the breast area in a mammogram: (a) before intensity range alignment, (b) after intensity range alignment. The staple-shaped red solid lines on the top of each histogram represent the intensity range of the fatty region, whereas the red arrows indicate the offset intensity, i_{off} . The range of the fatty region in each mammogram was that determined by the experts using an interactive thresholding.

$$\hat{f}(\mathbf{x}) = f(\mathbf{x}) - i_{off}, \quad \forall \mathbf{x} \in \Omega_B \quad (14)$$

In (13), M is a constant parameter specifying the minimum threshold of the histogram, which was set to 50 heuristically. Thus, this scheme seeks the value of i_{off} , the leading edge of the histogram within the breast area, Ω_B , which is then subtracted from all intensity values in Ω_B to provide the shift to the histogram. The resulting effect is shown in Fig. 4(b),

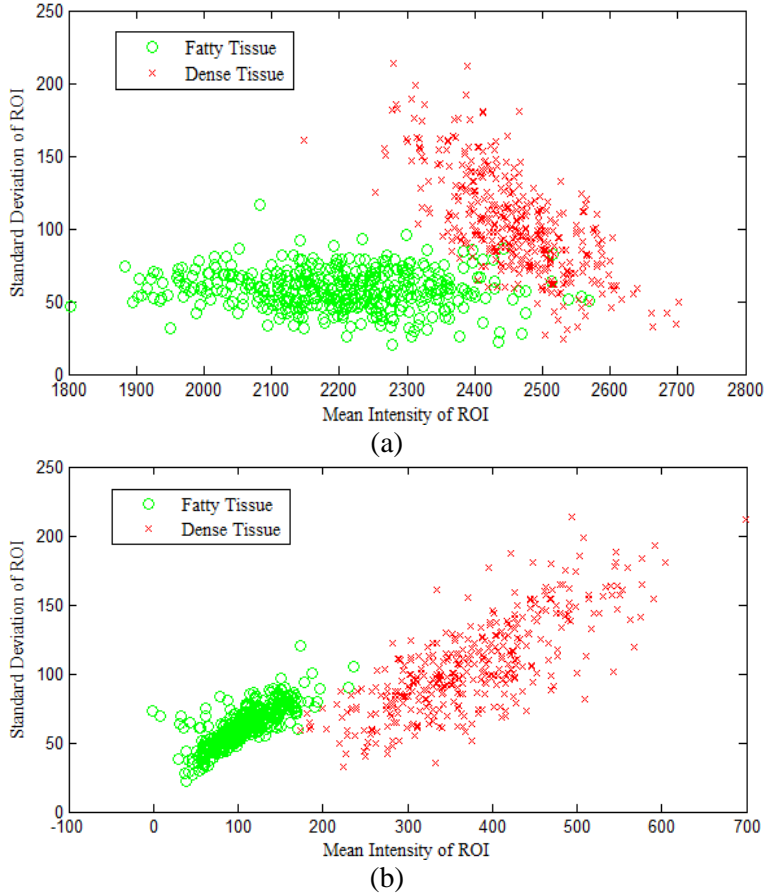


Figure 5. A 2D scatter plot of the mean and standard deviation of ROIs within fatty and dense regions: (a) before the histogram shift, (b) after the histogram shift.

where histograms of example mammograms are aligned to give much more consistent intensity values for the fatty regions as compared to those before the histogram shift. This type of intensity-aligned image $\hat{f}(\mathbf{x})$ was used for the subsequent processing. I further verified this intensity alignment effect with a selected set of mammograms by examining scatters of the local statistics within the ROIs, as defined by experts on fatty and dense tissue areas separately. The samples of 2D scatter plots in Fig. 5 are from the subset of training mammograms to visualize the effect of the histogram shift. Compared in Fig. 5(a) are 2D scatter plots of the local mean and the standard deviation before and after the histogram shift. This figure clearly shows that the intermixed distribution of the local statistics for the fatty and dense tissues in the original dataset shown in Fig. 5(a) are well separated after the application of the histogram shift operation as shown in Fig. 5(b).

3.5. PTPM Construction

This step constructs the PTPM, which was intended to capture the learned knowledge of experts, by extracting local statistics from user-defined ROIs on dense and fatty regions for the entire population of training mammograms. For the local statistics, the mean and standard deviation within the local ROI were utilized to account for the notion that fatty and dense regions are distinct in the X-ray attenuation and heterogeneity of the tissue composition [19]. In order to accurately obtain the ROIs of dense and fatty regions, I provided the experts with in-house software which allowed the experts to determine the

boundary between the two regions using an interactive thresholding technique. The breast area was first segmented automatically by applying the histogram modeling technique described in section 3.4; therefore, the experts could determine the boundary more conveniently. An example boundary drawn by an expert is depicted as the red solid line in Fig. 6(a).

Once the region boundary was determined by the experts, the ROIs

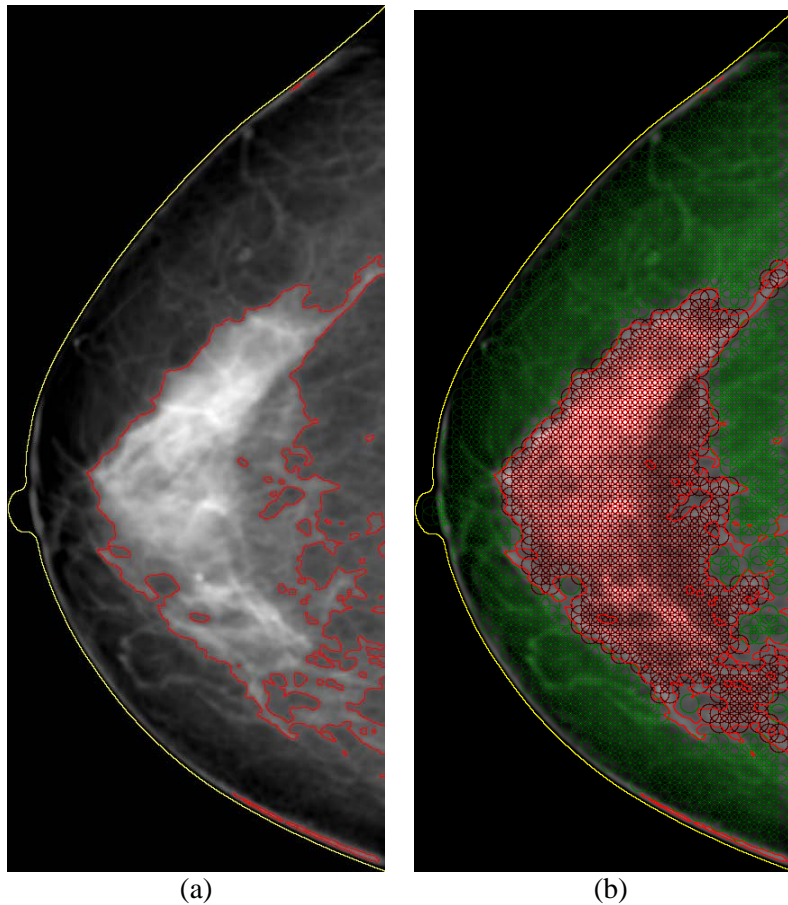


Figure 6. ROI selection in the breast area: (a) a preprocessed mammogram in which the boundaries of the breast area and dense regions are shown in a color overlay with yellow and red, and (b) the selected ROIs within dense and fatty regions marked as red and green circles.

for each tissue were defined automatically. I use the symbols Ω_D and Ω_F for the dense and fatty regions, respectively, such that $\Omega_D \cup \Omega_F = \Omega_B$ and $\Omega_D \cap \Omega_F = \emptyset$.

Next was the extraction of the statistical features. First, I defined the *local neighborhood* of a given pixel $\mathbf{x}_0 = (x_0, y_0)$ within a region.

$$B_r^k(\mathbf{x}_0) = \{\mathbf{x} \in \Omega_k \mid d(\mathbf{x}, \mathbf{x}_0) \leq r\} \quad (15)$$

$$n(B_r^k(\mathbf{x}_0) \cap \Omega_k) / n(B_r^k(\mathbf{x}_0)) > \kappa, 0 < \kappa \leq 1 \quad (16)$$

In (15)–(16), k is a subset indicator that can be either D or F , $d(\cdot)$ is the *Euclidean* distance measurement of two points, $n(\cdot)$ is the number of elements in the set, and κ is the portion that specifies the

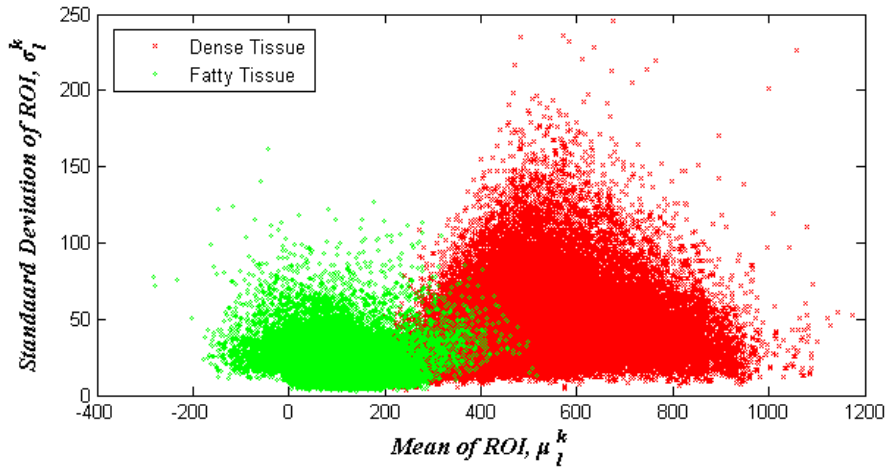


Figure 7. Scatter plot of the obtained statistical features from 297 mammograms (red: dense region, green: fatty region).

minimum number of elements in $B_r^k(\mathbf{x}_0)$ included in Ω_k . In other words, $B_r^k(\mathbf{x}_0)$ is referred to as a *closed ball* with radius r centered at \mathbf{x}_0 . Using the closed ball in (15) with respect to condition (16), the entire mammogram was scanned at an interval of r and the ROI satisfying condition (16) was assigned to either Ω_D or Ω_F , which were determined by the experts' segmentation results. The values of κ and r were set to 0.99 and 1 cm, respectively. ROIs that did not satisfy condition (16) were discarded. In Fig. 6(b), the selected ROIs of the dense and fatty region are overlaid on a mammogram as red and green circles, respectively. By utilizing the selected and class-determined ROIs, the mean and standard deviation within each ROI were computed by as follows:

$$\mu_l^k(\mathbf{x}) = \sum_{\mathbf{j} \in B_r^k(\mathbf{x})} \hat{f}(\mathbf{j}) / n(B_r^k(\mathbf{x})) \quad (17)$$

$$\sigma_l^k(\mathbf{x}) = \sum_{\mathbf{j} \in B_r^k(\mathbf{x})} \left(\hat{f}(\mathbf{j}) - \mu_l^k(\mathbf{x}) \right)^2 / \left(n(B_r^k(\mathbf{x})) - 1 \right), \quad (18)$$

In this equation, l denotes the index of each statistical feature to identify each training sample. Figure 7 shows a 2D scatter plot of the local statistics obtained from the entire population of the training mammogram set.

The obtained local statistics were used to estimate their probability density function (PDF) for the dense and fatty regions. I employed a nonparametric PDF estimation scheme termed *Parzen Window*, which is

particularly useful when no a priori information is available [45]. The PDF estimation was carried out according to (19).

$$\hat{p}^k(\mathbf{s}_i^k; h) = \frac{1}{N^k} \sum_{n=1}^{N^k} K(\mathbf{s}_i^k; \mathbf{s}_n^k, h). \quad (19)$$

In (23), $\mathbf{s}_i^k \in \mathbb{R}^2$ is a feature vector for which $\mathbf{s}_i^k = (\mu_i^k, \sigma_i^k)$; N^k is the total number of data points from a subset Ω_k , and $K(\cdot; \mathbf{s}_n^k, h)$ is a

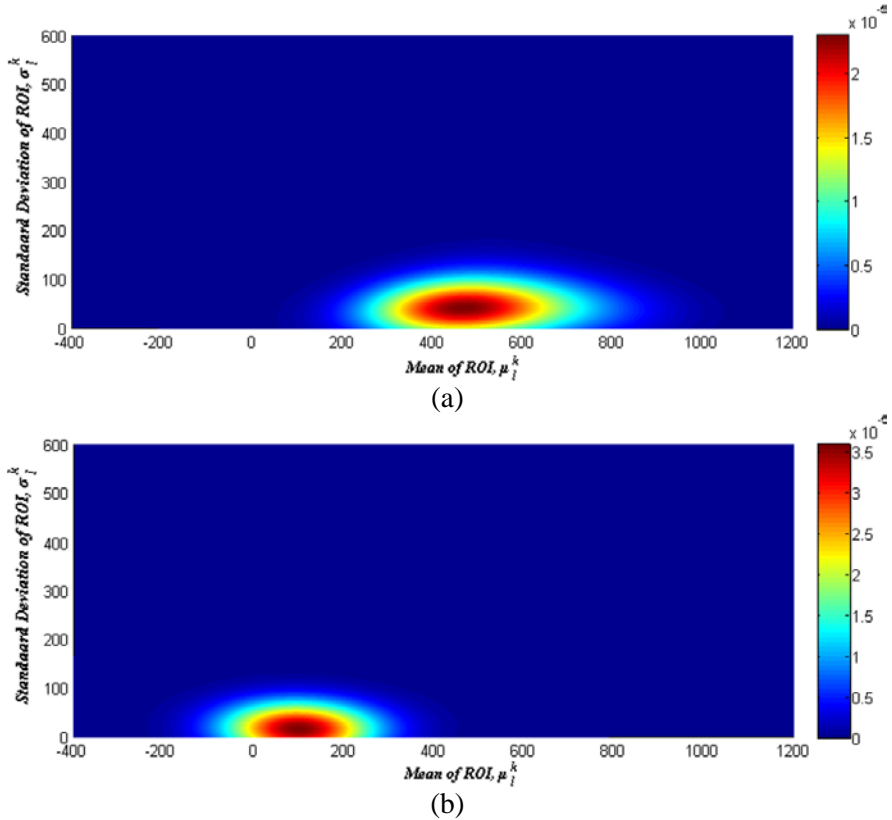


Figure 8. The calculated probability density function of (a) dense region, $\hat{p}^D(\mathbf{s})$, and (b) fatty region, $\hat{p}^F(\mathbf{s})$, by using non-parametric estimation scheme.

kernel function centered on \mathbf{s}_n^k with a window scale parameter h , in which a multivariate Gaussian basis function was used as the kernel with the window parameter $h=0.04$ according to Silverman's rule of thumb [46]. The estimated PDFs are shown in Fig. 8.

Finally, the class probabilities of the dense and fatty tissues were calculated for the entire feature space. As the class probability is, by definition, the measure for a feature vector to belong to the classes of dense and fatty tissue in this case, the class probabilities were simply calculated as the fractional PDFs as below.

$$C_D(\mathbf{s}) = \frac{\hat{p}^D(\mathbf{s})}{\hat{p}^D(\mathbf{s}) + \hat{p}^F(\mathbf{s})} \quad (20)$$

$$C_F(\mathbf{s}) = 1 - C_D(\mathbf{s}). \quad (21)$$

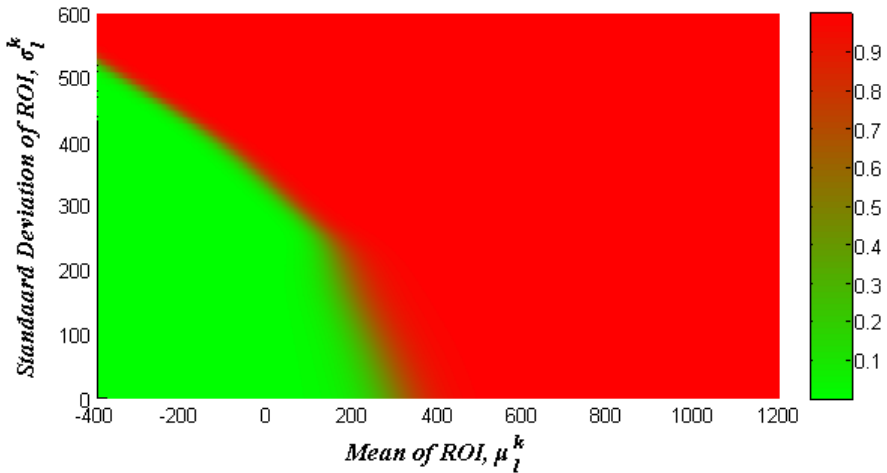


Figure 9. The PTPM obtained from the population of the dense region ($C_D(\mathbf{s})$) derived from the nonparametric probability density function.

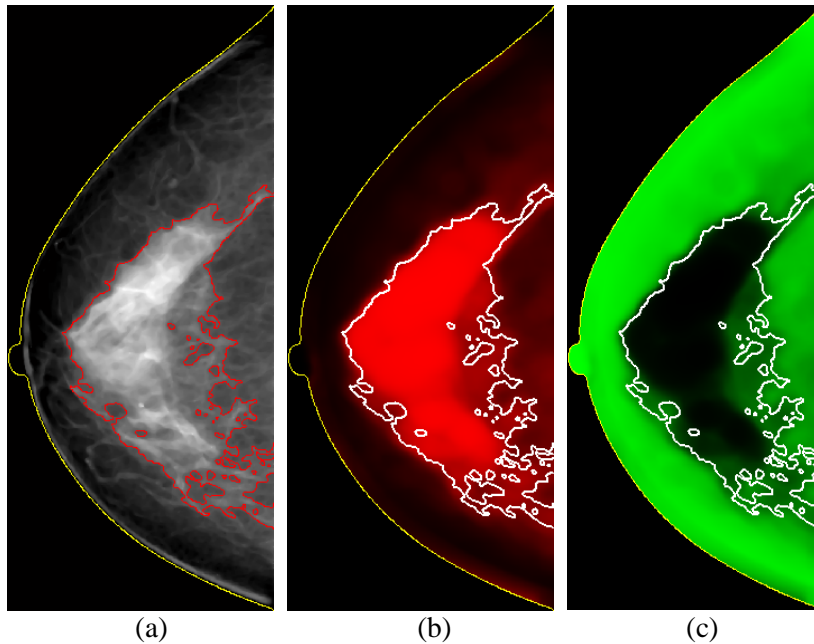


Figure 10. A pictorial example of the prior probability estimation result of a given mammogram: (a) the input mammogram, and (b)–(c) the probability of each pixel being a dense region $P_D(\mathbf{x})$ and a fatty region $P_F(\mathbf{x})$, respectively. Note that the color saturation level represents the probability value.

Figure 9 shows the finally obtained PTPM as a color map which represents the probability of the feature vector of an ROI to belong to a tissue class reflecting the knowledge learned from experts with the entire population of training mammograms.

3.6. Density Estimation

The PTPM generated in section 3.5 was utilized for the density estimation for a given mammogram. First, the given mammogram was preprocessed in the same way as described in section 3.4, with the subsequent calculation of the

local statistics (i.e., μ_i^k and σ_i^k) at each pixel within the breast area. Next, the class probabilities of dense and fatty tissues were computed using the PTPM shown in Fig. 9, as follows:

$$P_k(\mathbf{x}) = C_k(\mathbf{s}) = C_k(\mu(\mathbf{x}), \sigma(\mathbf{x})). \quad (22)$$

Figure 10 illustrates an example mammogram with the probabilities for dense tissue $P_D(\mathbf{x})$ and fatty tissue $P_F(\mathbf{x})$ mapped at each pixel as color overlays. The contour line from the experts' manual segmentation is given for a visual comparison. Note that this tissue probability map was created before proceeding to the level set segmentation step.

The PTPMs obtained with (22) were utilized in the motion equation (12) to guide the evolution of the contours toward the desired boundary between the dense and fatty region. Here, $P_D(\mathbf{x})$ and $P_F(\mathbf{x})$ replaced $P_+(\mathbf{x})$ and $P_-(\mathbf{x})$ in (12), respectively.

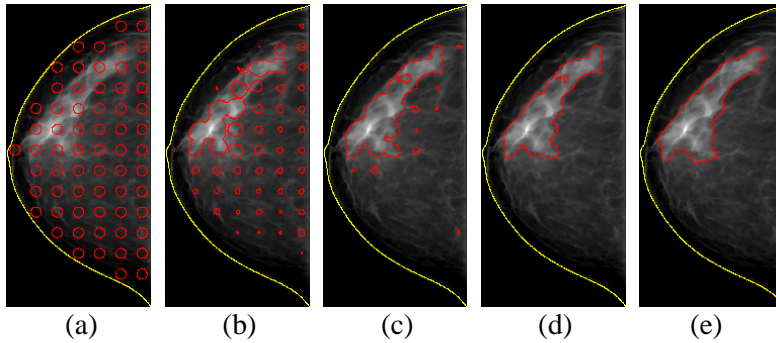


Figure 11. The evolution of contours at (a) 0, (b) 5, (c) 10, (d) 30, and (f) final iterations, respectively.

The contour was initialized with regular multiple circles inside the breast area, and the time evolution of the level set was terminated when the energy drop rate was reduced to a sufficiently small value K_{itr} or when the number of iterations reached a predetermined maximum count M_{itr} . The values of K_{itr} and M_{itr} were 0.001 and 300, respectively. Finally, the

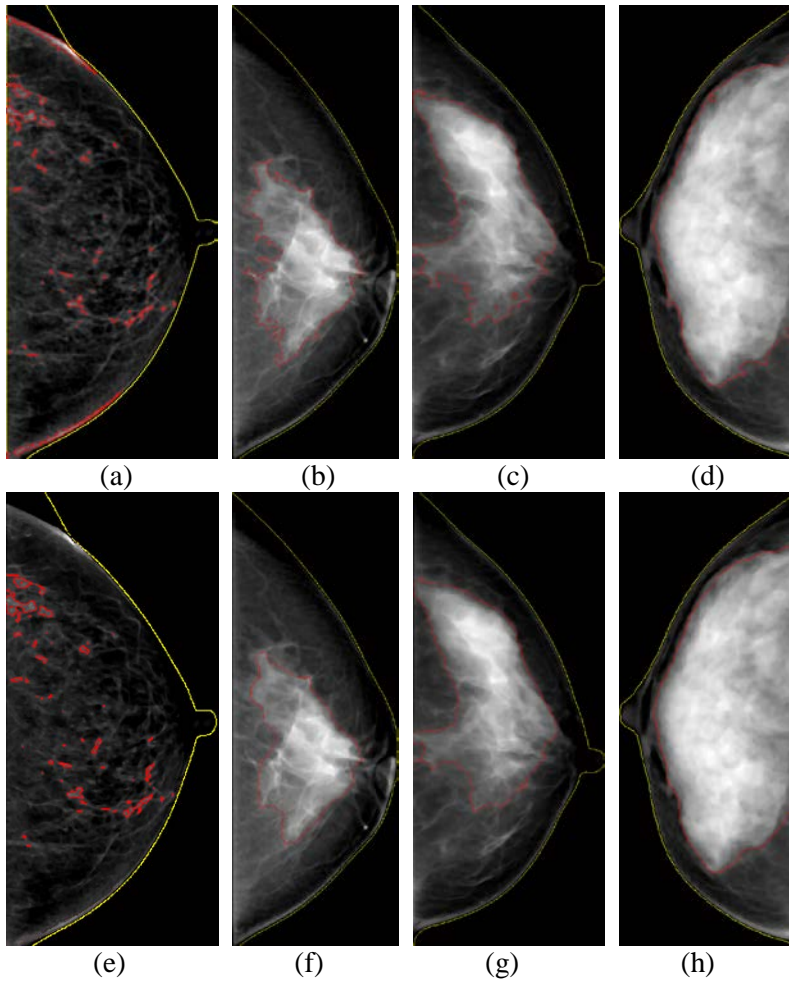


Figure 12. A comparison of the estimations between (top) the results of the interactive thresholding with the in-house software and (bottom) the outputs of the proposed method. The boundaries of the breast areas are denoted by the yellow solid line while those of the dense regions are depicted with the red solid line.

mammographic percent density (MPD) was calculated as follows:

$$MPD = \frac{|H(\hat{\phi})|}{n(\Omega_B)} \cdot 100\% \quad (23)$$

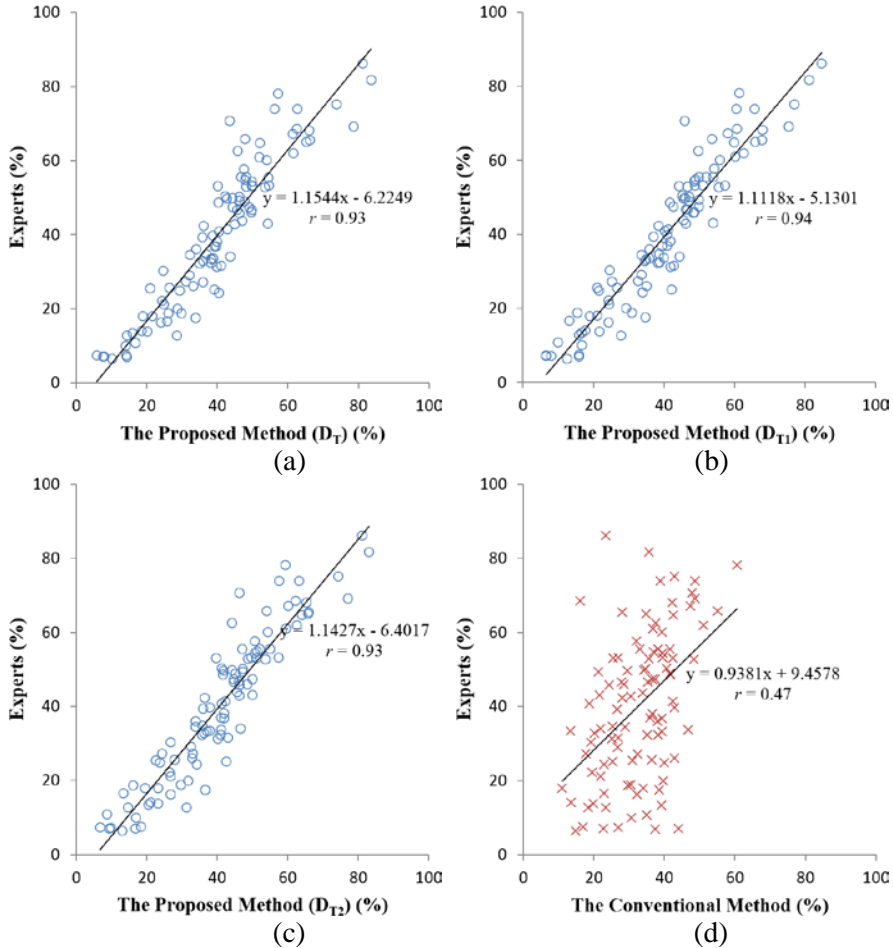


Figure 13. 2D scatter plots of the experts' estimation versus the automated estimation process using (a, b, and c) the proposed method against the experts; assessments, and (d) the CV level set method. The horizontal and vertical axes are MPD calculated by the automated methods and by the experts, respectively. The correlation coefficients are shown near the trend lines. Note that the result of the proposed method in (a) was trained with the entire training dataset, whereas the results in (b) and (c) were trained with the first and second training subsets.

4. RESULTS

4.1. Visual Assessment of Contours

A visual assessment of the final contours was made to verify if the contour evolution converged to appropriate locations.

The appropriateness of the contour was validated in terms of the location and extent of contours in comparison with those generated by the experts. Figure 11 shows the evolution of the contours captured at 0, 5, 10, 30, and at the final iterations for the selected mammograms. For all 100 mammograms, the final contours were found to be appropriate.

Figure 12 compares the final contour produced by the proposed method and the reference contour drawn by experts on the selected mammograms. This figure shows that the contours by the proposed method closely match those by the experts, even when there is a hazy transition between the two regions. Noteworthy is that the contours in the bottom row are smoother than those in the upper row while their overall shapes are well preserved.

4.2. Agreement with the Experts' Assessments

Three experts measured the density of 100 mammograms twice using the Cumulus4 software in order to examine the effect of intra-rater variation; thus, there were six measurements per mammogram.

For an evaluation of the accuracy, a reference measurement set was established by averaging the six measurements from the three experts for each

test mammogram.

For comparison purposes, the performance of a conventional level set was also evaluated. The conventional level set in this study refers to the CV model.

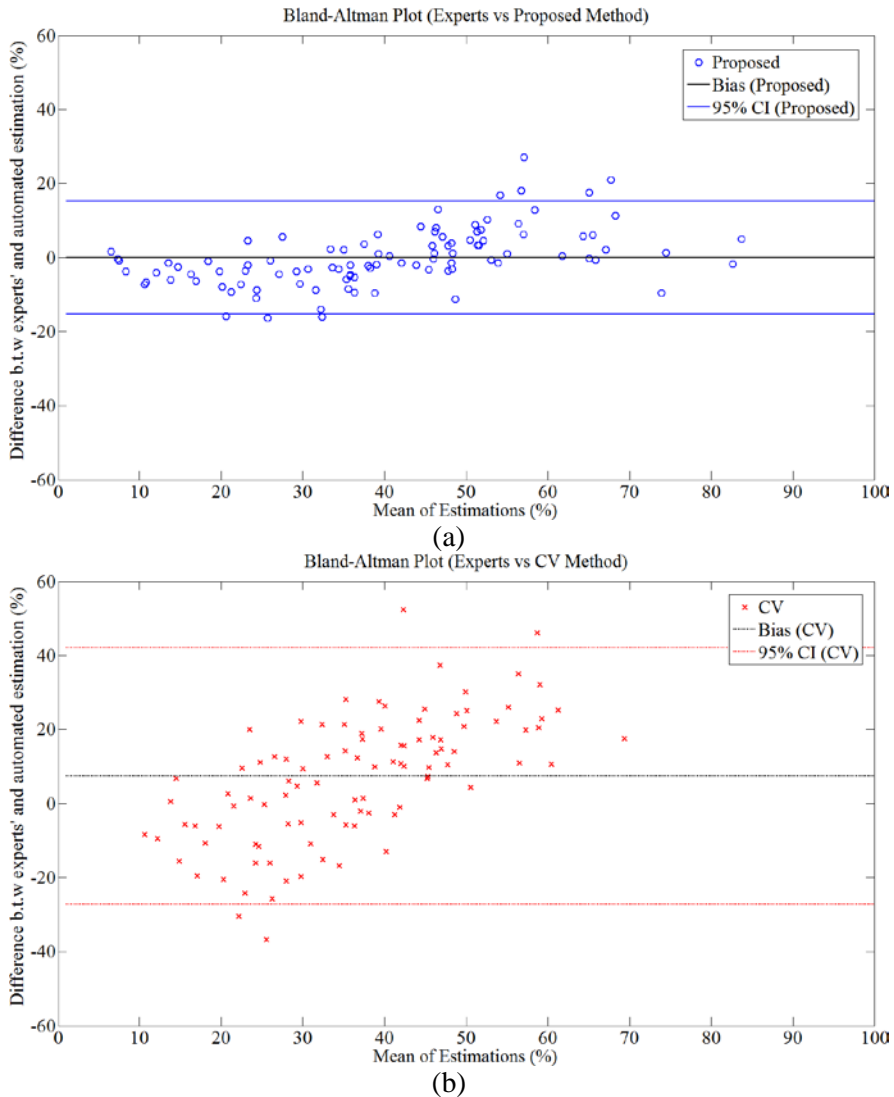


Figure 14. Bland-Altman plot of the experts' assessments against the (a) proposed and (b) conventional methods. The horizontal and vertical axes are the mean of two estimations and difference between the experts' and automated estimation, respectively.

Scatter plots between the automated measurements and the reference

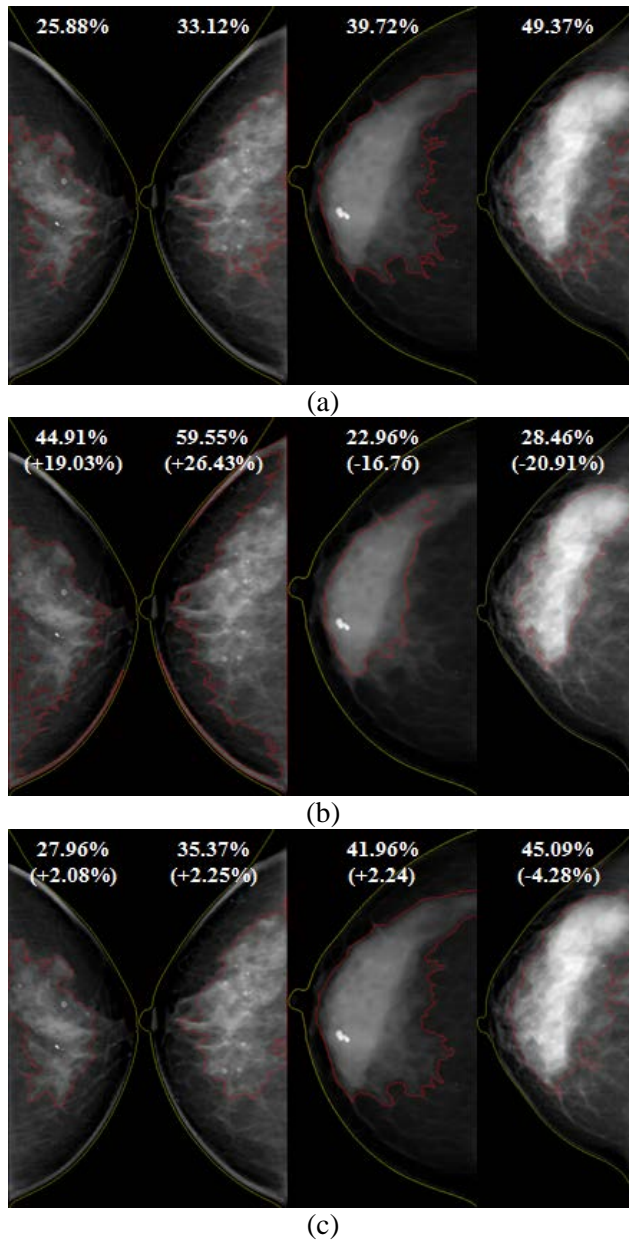


Figure 15. Example mammograms with a hazy transition of the pixel intensities from fatty to dense regions, where the estimated mammographic percent density is shown on the top of each segmentation result: (a) the reference estimate from the radiologists, and estimates with (b) the CV method and (c) the proposed method. Note that the deviations from the reference estimates are shown in parentheses below the percent density.

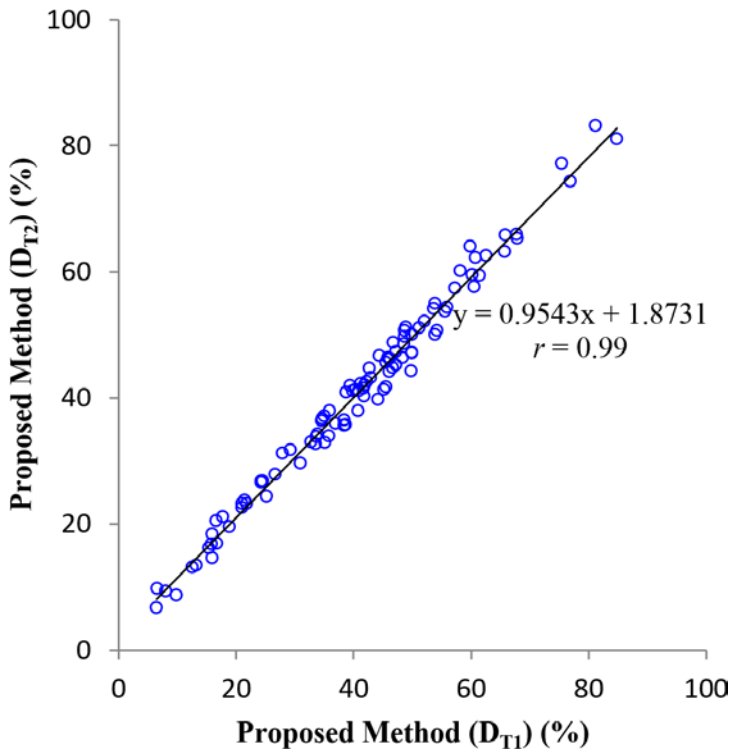


Figure 16. A 2D scatter plot of estimation results by the proposed method trained with D_{T_1} versus D_{T_2} .

measurements are shown in Fig. 13. Note that the data points in Fig. 13(a)-(c) of the proposed method are quite compactly distributed near the trend lines, while those in Fig. 13(d) of the CV method are much more scattered. The correlation coefficients of the proposed methods with D_T , D_{T_1} , and D_{T_2} were 0.93, 0.94, and 0.93, respectively, while that of the CV method was 0.47.

Bland-Altman plots are depicted in Fig. 14, in which the mean difference is shown as a black line in the middle of the plot and the limits of agreement are drawn as blue lines. The moderate systematic trend observed in Fig. 14(b), with the CV method, is mostly removed in Fig. 14(a) with the proposed method. As summarized in Table II, the standard deviation of the

TABLE II. A comparison of the results between the radiologists' interactive estimation results using the in-house software and the outputs of the proposed method.

Method	Correlation Coefficient	Mean Diff. (%)	Std. Dev. of Diff. (%)
Proposed (D_T)	0.93	-0.01	7.76
Proposed (D_{T_1})	0.94	-0.57	6.80
Proposed (D_{T_2})	0.93	-0.58	7.54
Chan-Vese	0.46	7.43	17.72

difference for the proposed method ranged from 6.80 to 7.76, while that for the CV method was 17.72. This demonstrates the higher precision of the proposed method.

Figure 15 shows the segmented contours and density estimates by the conventional level set and by the proposed method in comparison with the reference results for the selected mammograms, showing relatively large discrepancies. While the conventional level set produced a wide range of discrepancies ranging from -16.76 to +26.43, the proposed method greatly narrowed the range from -4.28 to +2.25. Note that even for those difficult cases in which a very haze intensity transition existed between the two regions, the contours by the proposed method generally agree well with the reference contours, whereas the contours by the conventional level set converged to a false boundary having a steeper transition.

Depicted in Fig. 16 is a 2D scatter plot comparing two measurements of the proposed method using the partial PTPMs generated with D_{T_1} and with D_{T_2} . The plots are very compactly located near the trend

lines and were excellently correlated ($r= 0.99$), verifying the robustness of the proposed method against the population dependence of PTPM training.

4.3. Evaluation on Various ROI Scales

In this subsection, the effects of various ROI size on the performance are evaluated. For this, I set the ROI size from 4mm to 30mm and constructed the PTPM for each ROI size. Figure 17 depicts the 2D scatter plot between the estimation results of radiologists and the proposed method, and the agreement with respect to the ROI size is shown in Fig. 18, in which the performance began dropping with the ROI size larger than 10mm.

4.4. Effect of the Proposed Procedures

In order to investigate the effect of the PTPM-based level set method, the performance was evaluated with following subjects: no histogram shift, large ROI, conventional level set method, thresholding on statistical samples, thresholding on PTPM, and PTPM-based level set method.

First of all, the performance of PTPM-based level set method without the histogram shift, explained in section 3.4, was evaluated to investigate the effect of the histogram shift. In addition, to determine the threshold within the 2D statistical samples, shown in Fig 7, I utilized the support vector machine (SVM) technique, while the MPD calculation by only using PTPM was conducted in which the pixels have the prior probability, illustrated in Fig. 10(b), higher than 0.5 were assigned as dense region. As

shown in Fig. 19, the performances were varied regarding various approaches. Note, here, that the performance became better as the proposed procedures were included with the proposed order in this study.

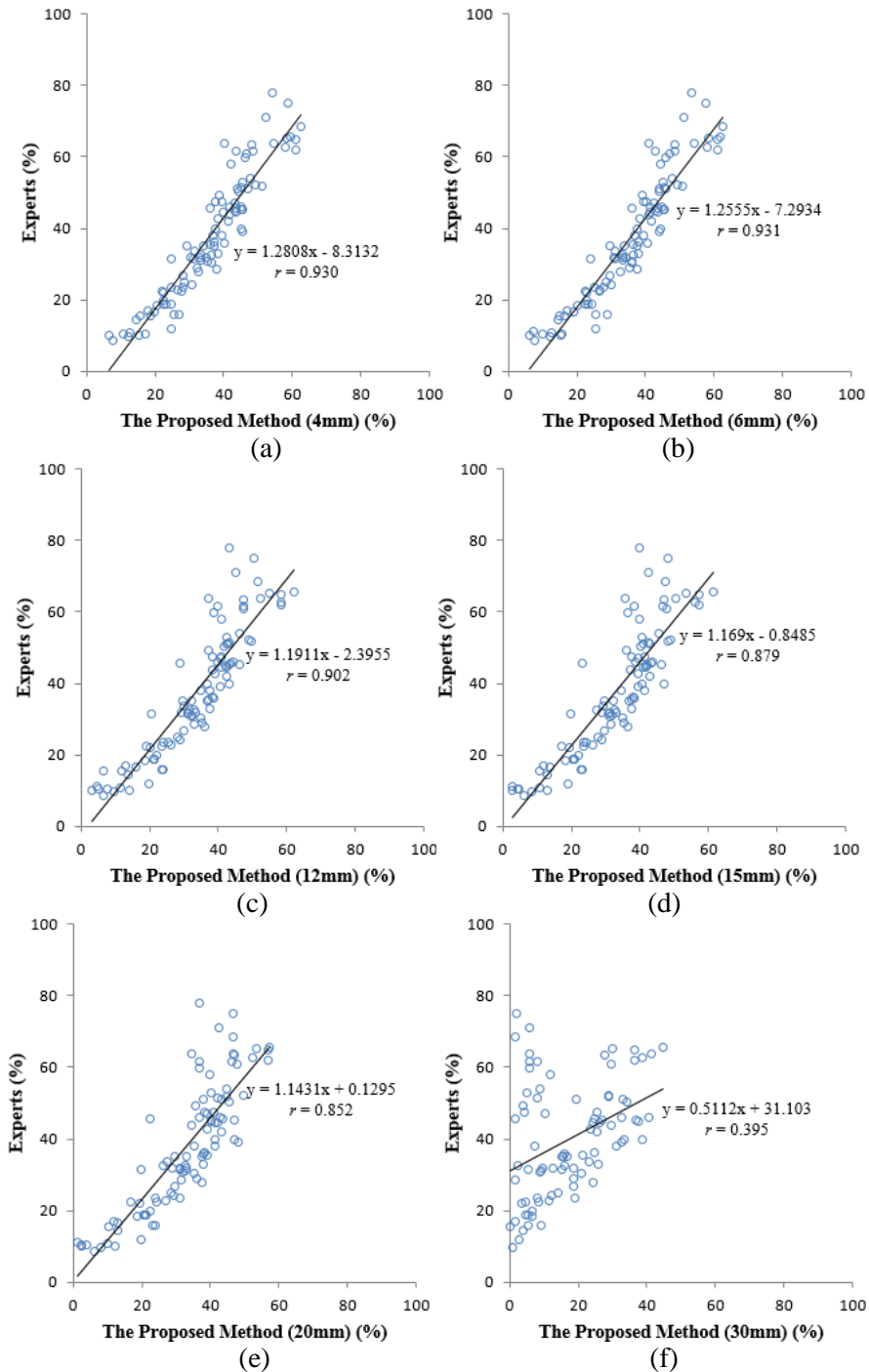


Figure 17. 2D scatter plots of the experts' estimation versus the automated estimation process using ROI size of (a) 4mm, (b) 6mm, (c) 12mm, (d) 15mm, (e) 20mm, and (f) 30mm.

5. DISCUSSION

This study aimed to develop a novel fully automated image segmentation method which enables accurate estimations of mammographic density levels by incorporating learned knowledge from experts into a level set framework.

As pointed out in previous studies, a major difficulty when automatically segmenting dense regions in a mammogram, especially for area-based estimations, lies in the determination of a boundary on a hazy transition zone from a fatty to a dense region where the intensity range of the two regions largely overlaps and does not show sufficient contrast. This property stems from the fact that mammography is a projection of superimposed tissues consisting of different structures. This unique property makes it difficult to apply conventional segmentation techniques, such as the Chan-Vese method, which are based on a simple image model assuming that the two regions are piecewise-constant or have separable histograms.

The motivation of this study was the notion that an expert could segment out a dense region even with extremely difficult mammograms and that the incorporation of learned knowledge into a segmentation method can, therefore, lead to a novel method that can overcome the known challenges.

In this study, I captured the learned knowledge from experts by extracting the local statistics of both dense and fatty regions in a mammogram set of a patient population and constructed a PTPM which was in turn incorporated into a level set framework. Although I utilized the mean and standard deviation as ROI statistics, additional texture features could be

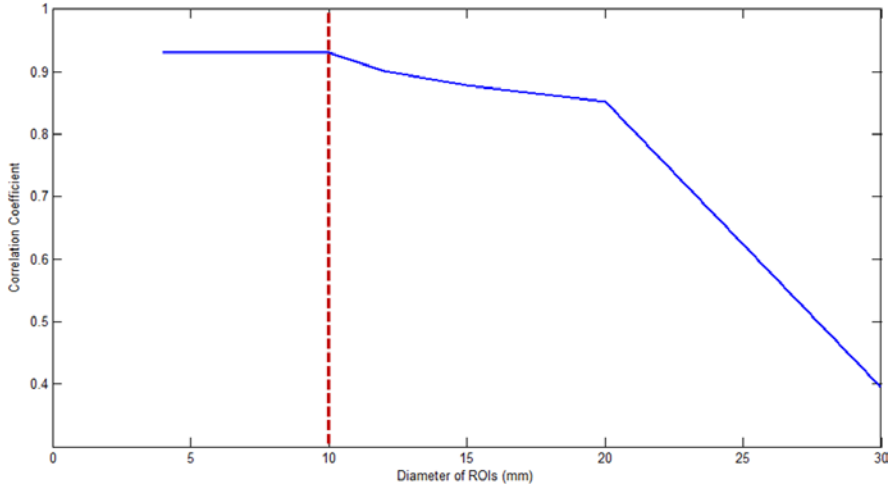


Figure 18. The performance graph with respect to various ROI sizes. The dashed line indicates the performance of the proposed method with ROI size utilized in this study (10mm).

regarded, such as skewness, kurtosis, or the structure tensor. Figure 17 shows an example case in which the learned knowledge is not fully captured resulting in a slight under-estimation of the proposed method compared to the experts' estimation.

On the other hand, in estimating the PDF with the local statistics of finite measurements, I employed the nonparametric PDF estimation scheme termed *Parzen Window*, which is particularly attractive when there is no guarantee that the PDF will follow a parametric function [45]. In fact, I found that the fitted Gaussian PDFs using the maximum likelihood estimation (MLE) method produced large errors, particularly at the transition zone, where the local statistics were only sparsely sampled. I believe the improved accuracy in estimating the PDFs using this nonparametric scheme partly contributed to the high performance overall of the proposed method.

In my quantitative evaluation experiment, the proposed method

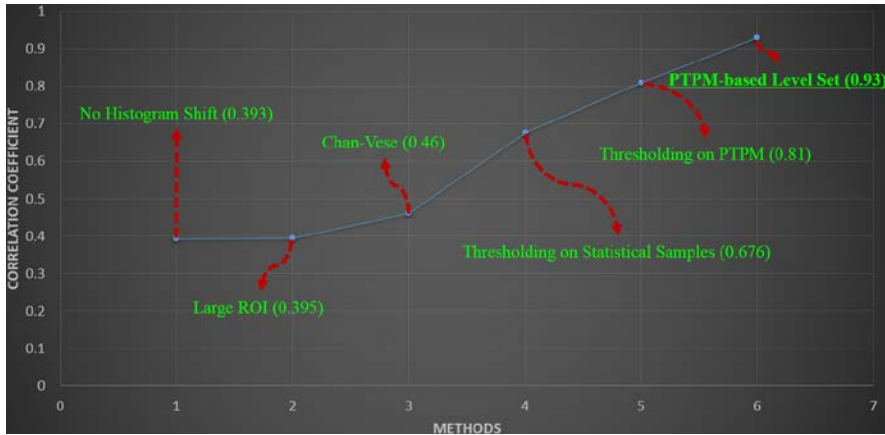


Figure 19. The effect of the proposed order of procedures in this study.

produced a Pearson correlation coefficient of 0.93, which ranks as one of the highest values considering the performance levels reported in previous studies, which ranged from 0.67 to 0.94 [16, 24, 41].

I attribute this high performance to its ability to accomplish a robust segmentation task for diverse types of mammograms with a wide range of percent densities of 5.5% to 83%. For example, in the preliminary study, even human readers who did not have sufficient training could not accomplish appropriate segmentation for a subset of mammograms having hazy transitions of pixel intensities from fatty to dense regions (examples of such cases are shown in Fig. 15), and Conant *et al.*[47] also report that clinically trained readers ($r=0.91$) show higher agreement than non-clinically trained readers ($r=0.83$). In this sense, the proposed method outperformed ordinary human observers as well as conventional segmentation methods at least in a subset of difficult cases. Considering the limitations of previous methods, in which outliers were inevitably produced and led to a degradation of the overall performance and reliability, the robustness shown in the experimental

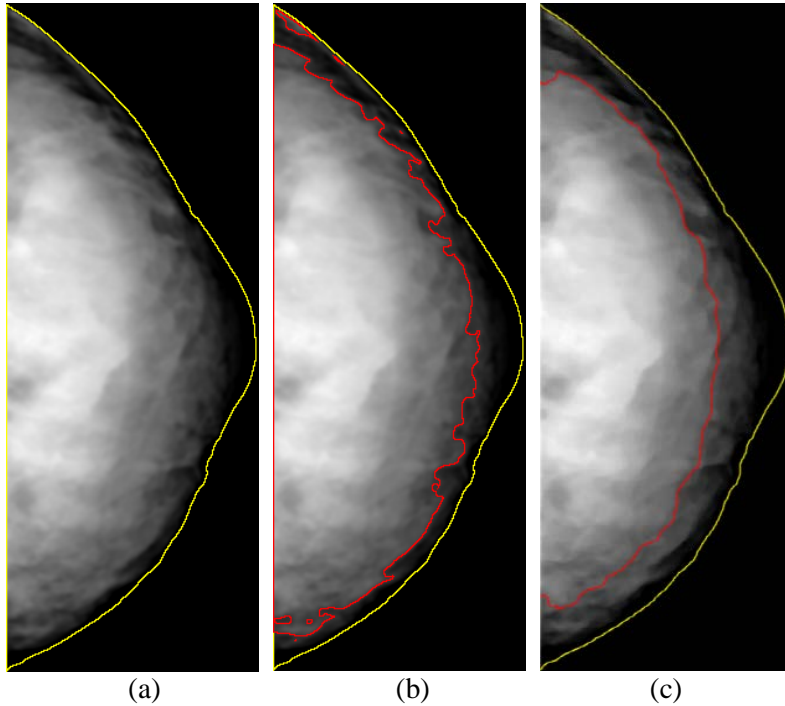


Figure 20. An example case where the estimation result of proposed method disagreed with that of experts: (a) original mammogram with automated extraction of breast region, (b) result of experts' interactive thresholding, (c) automated estimation result of the proposed method.

results can be regarded as a unique strength of the proposed method. In fact, Zhou *et al.*[17] reported that a small subset of outlying mammograms showed a degraded overall correlation performance of 0.746, though it could be as high as 0.94 without the outliers.

Incorporating learned knowledge into a segmentation scheme has been a subject of active research in recent years. Gloger *et al.*[48] proposed the incorporation of prior shapes into a level set by generating a probability map of a kidney from a manually segmented MR data set. Zhang *et al.*[49] applied a dictionary learning approach via the sparse representation of a manually labeled data set to the deformable segmentation of lungs in

radiographs and livers in 3D MR images. Much earlier, Paragios and Deriche[40] incorporated the prior probability of a patch-based feature vector into a geodesic active region model for texture segmentation. Common to these studies and the proposed method is the motivation to incorporate the ability of the human visual system, in which learned knowledge is used to achieve the effective segmentation of ambiguous objects into a computerized image segmentation scheme, thereby, improving the performance. A unique challenge in my study was to extract the learned knowledge of an expert reader, which is devoid in our innate human visual system and which is attainable only through appropriate training. Distinguishing a dense region from the surrounding fatty tissue was only achieved through multiple sessions of training for the participants in my preliminary experiment. Considering the fact that the segmentation target in most previous studies was within the ambiguity level resolvable by the innate human visual system, the segmentation task as part of a mammographic density estimation was regarded as having a higher level of ambiguity.

Hence, the contribution of this study is twofold: 1) I could successfully incorporate the learned knowledge of expert readers into the segmentation scheme, and 2) the developed method showed a performance level equivalent to that of expert human observers.

Contrary to the image- and area-based mammographic density estimation, there are techniques which provide physical parameter-based calibrations of mammograms and estimations of breast densities by exploiting physical imaging variables including the tube voltage, exposure, and the

thickness of the compressed breast [29, 30, 32, 36]. These techniques explicitly require raw mammograms, but most medical centers maintain vendor-specific post-processed mammograms, which are mainly used for diagnosis in order to save storages; therefore, it could be difficult for them to be applied for large retrospective studies. Furthermore, in practice, the errors of the physical parameters and the complex physical phenomena involved in X-rays to matter interaction may limit the accuracy and the related estimates. On the other hand, some of the techniques above provided volumes of breasts and dense regions by using estimated planar measure and the compressed breast thickness, so, in principle, they may provide additional information for breast density estimates [29, 30, 32]. Nevertheless, a recent study reported that area-based mammographic density estimates were more closely associated with breast cancer risk than volume-based estimates [14]. Thus, I believe that the image- and area-based measure will remain in widespread use due to the associated levels of convenience and intuitiveness, even when the shortcomings of the volume-based methods are overcome.

This study still has several limitations in that only CC-view mammograms were used, while MLO views are also obtained in standard mammographic examinations. As MLO-view mammograms contain information on breast tissues projected at a different angle, estimating the breast density using both CC- and MLO-view mammograms has the potential to improve the level of reliability even more.

Moreover, I used images acquired with a single equipment model (i.e., Senographe 2000D, GE). As each type of mammographic equipment has

different imaging characteristics and post-processing options, the study results cannot be directly applied to mammograms obtained with other types of equipment. Therefore, adapting the proposed method to the imaging characteristics of different equipment models and preprocessing options is warranted as the next step of this research.

6. CONCLUSIONS

I have developed a novel image segmentation method which enables accurate estimations of mammographic density levels by incorporating learned knowledge from experts into a level set framework. The learned knowledge was captured in the form of a PTPM with the use of local statistics within manually drawn segmentation results and was used in the level set framework as a control term to guide the evolution to converge to the desired boundary. This result suggests that the proposed method successfully incorporated the learned knowledge of the experts' visual systems and that it has the potential to be used as an automated and quantitative tool for estimations of mammographic breast density levels.

REFERENCES

1. Warner, E., Lockwood, G., Math, M., Tritchler, D., and Boyd, N.F. (1992). The Risk of Breast-Cancer Associated with Mammographic Parenchymal Patterns - a Metaanalysis of the Published Literature to Examine the Effect of Method of Classification. *Cancer Detect. Prev.* 16, 67-72.
2. Boyd, N.F., Guo, H., Martin, L.J., Sun, L.M., Stone, J., Fishell, E., Jong, R.A., Hislop, G., Chiarelli, A., Minkin, S., et al. (2007). Mammographic density and the risk and detection of breast cancer. *N. Engl. J. Med.* 356, 227-236.
3. Harvey, J.A., and Bovbjerg, V.E. (2004). Quantitative assessment of mammographic breast density: Relationship with breast cancer risk. *Radiology* 230, 29-41.
4. Lundstrom, E., Wilczek, B., von Palffy, Z., Soderqvist, G., and von Schoultz, B. (1999). Mammographic breast density during hormone replacement therapy: Differences according to treatment. *Am. J. Obstet. Gynecol.* 181, 348-352.
5. Cil, T., Fishell, E., Hanna, W., Sun, P., Rawlinson, E., Narod, S.A., and McCready, D.R. (2009). Mammographic Density and the Risk of Breast Cancer Recurrence After Breast-Conserving Surgery. *Cancer* 115, 5780-5787.
6. Habel, L.A., Dignam, J.J., Land, S.R., Salane, M., Capra, A.M., and Julian, T.B. (2004). Mammographic density and breast cancer after ductal carcinoma in situ. *J Natl Cancer I* 96, 1467-1472.
7. Wolfe, J.N. (1976). Risk for Breast-Cancer Development Determined by Mammographic Parenchymal Pattern. *Cancer* 37, 2486-2492.
8. Habel, L.A., Capra, A.M., Achacoso, N.S., Janga, A., Acton, L., Puligandla, B., and Quesenberry, C.P. (2010). Mammographic Density and Risk of Second Breast Cancer after Ductal Carcinoma In situ. *Cancer Epidem Biomar* 19, 2488-2495.
9. D'Orsi, C.J., American College of Radiology., and American College of Radiology. BI-RADS Committee. (1998). Illustrated breast imaging reporting and data system (illustrated BI-RADS), 3rd Edition, (Reston, VA: American College of Radiology).
10. Nicholson, B.T., LoRusso, A.P., Smolkin, M., Bovbjerg, V.E., Petroni, G.R., and Harvey, J.A. (2006). Accuracy of assigned BI-RADS breast density category definitions. *Acad. Radiol.* 13, 1143-1149.
11. Kerlikowske, K., Grady, D., Barclay, J., Frankel, S.D., Ominsky, S.H., Sickles, E.A., and Ernster, V. (1998). Variability and accuracy in mammographic interpretation using the American College of Radiology Breast Imaging Reporting and Data System. *J Natl Cancer I* 90, 1801-1809.
12. Byng, J.W., Boyd, N.F., Fishell, E., Jong, R.A., and Yaffe, M.J. (1994). The Quantitative-Analysis of Mammographic Densities. *Phys Med Biol* 39, 1629-1638.

13. McCormack, V.A., and Silva, I.D.S. (2006). Breast density and parenchymal patterns as markers of breast cancer risk: A meta-analysis. *Cancer Epidem Biomar* 15, 1159-1169.
14. Boyd, N.F., Martin, L.J., Bronskill, M., Yaffe, M.J., Duric, N., and Minkin, S. (2010). Breast Tissue Composition and Susceptibility to Breast Cancer. *J Natl Cancer I* 102, 1224-1237.
15. Yaffe, M.J. (2008). Mammographic density - Measurement of mammographic density. *Breast Cancer Res* 10.
16. Karssemeijer, N. (1998). Automated classification of parenchymal patterns in mammograms. *Phys Med Biol* 43, 365-378.
17. Zhou, C., Chan, H.P., Petrick, N., Helvie, M.A., Goodsitt, M.M., Sahiner, B., and Hadjiiski, L.M. (2001). Computerized image analysis: Estimation of breast density on mammograms. *Med Phys* 28, 1056-1069.
18. Martin, K.E., Helvie, M.A., Zhou, C., Roubidoux, M.A., Bailey, J.E., Paramagul, C., Blane, C.E., Klein, K.A., Sonnad, S.S., and Chan, H.P. (2006). Mammographic density measured with quantitative computer-aided method: Comparison with radiologists' estimates and BI-RADS categories. *Radiology* 240, 656-665.
19. Heine, J.J., and Velthuisen, R.P. (2000). A statistical methodology for mammographic density detection. *Med Phys* 27, 2644-2651.
20. Saha, P.K., Udupa, J.K., Conant, E.F., Chakraborty, D.P., and Sullivan, D. (2001). Breast tissue density quantification via digitized mammograms. *Ieee T Med Imaging* 20, 792-803.
21. Glide-Hurst, C.K., Duric, N., and Littrup, P. (2007). A new method for quantitative analysis of mammographic density. *Med Phys* 34, 4491-4498.
22. Oliver, A., Freixenet, J., Marti, R., Pont, J., Perez, E., Denton, E.R.E., and Zwiggelaar, R. (2008). A novel breast tissue density classification methodology. *Ieee T Inf Technol B* 12, 55-65.
23. Keller, B., Nathan, D., Wang, Y., Zheng, Y., Gee, J., Conant, E., and Kontos, D. (2011). Adaptive multi-cluster fuzzy C-means segmentation of breast parenchymal tissue in digital mammography. *Medical image computing and computer-assisted intervention : MICCAI ... International Conference on Medical Image Computing and Computer-Assisted Intervention* 14, 562-569.
24. Keller, B.M., Nathan, D.L., Wang, Y., Zheng, Y.J., Gee, J.C., Conant, E.F., and Kontos, D. (2012). Estimation of breast percent density in raw and processed full field digital mammography images via adaptive fuzzy c-means clustering and support vector machine segmentation. *Med Phys* 39, 4903-4917.
25. Oliver, A., Llado, X., Perez, E., Pont, J., Denton, E.R.E., Freixenet, J., and Marti, J. (2010). A Statistical Approach for Breast Density Segmentation. *J. Digit. Imaging* 23, 527-537.
26. Kallenberg, M.G.J., Lokate, M., van Gils, C.H., and Karssemeijer, N. (2011). Automatic breast density segmentation: an integration of different approaches. *Phys Med Biol* 56, 2715-2729.
27. Kaufhold, J., Thomas, J.A., Eberhard, J.W., Galbo, C.E., and Trotter, D.E.G. (2002). A calibration approach to glandular tissue composition

- estimation in digital mammography. *Med Phys* 29, 1867-1880.
28. Malkov, S., Wang, J., Kerlikowske, K., Cummings, S.R., and Shepherd, J.A. (2009). Single x-ray absorptiometry method for the quantitative mammographic measure of fibroglandular tissue volume. *Med Phys* 36, 5525-5536.
 29. van Engeland, S., Snoeren, P.R., Huisman, H., Boetes, C., and Karssemeijer, N. (2006). Volumetric breast density estimation from full-field digital mammograms. *Ieee T Med Imaging* 25, 273-282.
 30. Highnam, R., Pan, X., Warren, R., Jeffrey, M., Smith, G.D., and Brady, M. (2006). Breast composition measurements using retrospective standard mammogram form (SMF). *Phys Med Biol* 51, 2695-2713.
 31. Lu, L.J.W., Nishino, T.K., Khamapirad, T., Grady, J.J., Leonard, M.H., and Bruner, D.G. (2007). Computing mammographic density from a multiple regression model constructed with image-acquisition parameters from a full-field digital mammographic unit. *Phys Med Biol* 52, 4905-4921.
 32. Pawluczyk, O., Augustine, B.J., Yaffe, M.J., Rico, D., Yang, J.W., Mawdsley, G.E., and Boyd, N.F. (2003). A volumetric method for estimation of breast density on digitized screen-film mammograms. *Med Phys* 30, 352-364.
 33. Heine, J.J., and Behera, M. (2006). Effective x-ray attenuation measurements with full field digital mammography. *Med Phys* 33, 4350-4366.
 34. Highnam, R., Brady, S., Yaffe, M., Karssemeijer, N., and Harvey, J. (2010). Robust Breast Composition Measurement - VolparaTM. In *Digital Mammography*, Volume 6136, J. Martí, A. Oliver, J. Freixenet and R. Martí, eds. (Springer Berlin Heidelberg), pp. 342-349.
 35. Heine, J.J., Cao, K., and Beam, C. (2009). Cumulative sum quality control for calibrated breast density measurements. *Med Phys* 36, 5380-5390.
 36. Heine, J.J., Cao, K., Rollison, D.E., Tiffenberg, G., and Thomas, J.A. (2011). A Quantitative Description of the Percentage of Breast Density Measurement Using Full-field Digital Mammography. *Acad. Radiol.* 18, 556-564.
 37. Fowler, E.E., Sellers, T.A., Lu, B., and Heine, J.J. (2013). Breast Imaging Reporting and Data System (BI-RADS) breast composition descriptors: Automated measurement development for full field digital mammography. *Med Phys* 40.
 38. Osher, S., and Sethian, J.A. (1988). Fronts Propagating with Curvature-Dependent Speed - Algorithms Based on Hamilton-Jacobi Formulations. *J Comput Phys* 79, 12-49.
 39. Mumford, D., and Shah, J. (1989). Optimal Approximations by Piecewise Smooth Functions and Associated Variational-Problems. *Commun Pur Appl Math* 42, 577-685.
 40. Paragios, N., and Deriche, R. (2002). Geodesic active regions and level set methods for supervised texture segmentation. *Int J Comput Vision* 46, 223-247.

41. Chan, T.F., and Vese, L.A. (2001). Active contours without edges. *IEEE T Image Process* 10, 266-277.
42. Brechtken-Manderscheid, U. (1991). Introduction to the calculus of variations, (London ; New York: Chapman & Hall).
43. Goldstraw, E.J., Castellano, I., Ashley, S., and Allen, S. (2010). The effect of Premium View post-processing software on digital mammographic reporting. *Brit J Radiol* 83, 122-128.
44. Bakic, P.R., Carton, A.K., Kontos, D., Zhang, C.P., Troxel, A.B., and Maidment, A.D.A. (2009). Breast Percent Density: Estimation on Digital Mammograms and Central Tomosynthesis Projections. *Radiology* 252, 40-49.
45. Parzen, E. (1962). Estimation of a Probability Density-Function and Mode. *Ann Math Stat* 33, 1065.
46. Silverman, B.W. (1986). Density estimation for statistics and data analysis, (London ; New York: Chapman and Hall).
47. Conant, E.F., Li, D., Gavenonis, S., Bakic, P.R., Carton, A.-K., Zhang, C., Maidment, A.D.A., and Kontos, D. (2010). A comparative study of the inter-reader variability of breast percent density estimation in digital mammography: potential effect of reader's training and clinical experience. In *Proceedings of the 10th international conference on Digital Mammography*. (Girona, Spain: Springer-Verlag), pp. 114-120.
48. Gloger, O., Tonnie, K.D., Liebscher, V., Kugelmann, B., Laqua, R., and Volzke, H. (2012). Prior Shape Level Set Segmentation on Multistep Generated Probability Maps of MR Datasets for Fully Automatic Kidney Parenchyma Volumetry. *IEEE T Med Imaging* 31, 312-325.
49. Zhang, S.T., Zhan, Y.Q., and Metaxas, D.N. (2012). Deformable segmentation via sparse representation and dictionary learning. *Med Image Anal* 16, 1385-1396.

Abstract in Korean

서론: 유방 X 선 영상에서의 밀도 측정을 자동화하는데 있어 어려운 점은 유방 X 선 영상이 3 차원 조직의 2 차원 투영영상이라는 것이며, 이러한 특성으로 인해 유관조직과 지방조직 사이의 경계가 모호하여 일반적인 영상처리 방법으로는 정확한 경계지점을 찾는 것에 한계가 있다. 따라서 본 연구에서는 전문가들로부터 획득한 사전 통계 정보를 학습과정을 거쳐 효과적으로 유방 밀도를 측정하는 방법을 제안한다.

방법: 총 349 명의 환자들로부터 획득한 397 장의 유방 X 선 영상 중 297 장의 영상을 활용하여 전문가들로부터 반자동 유방 측정 결과를 얻고 이 측정 결과로부터 통계적 조직 확률 모델을 학습한다. 입력으로 측정하고자 하는 영상이 들어오면 앞서 학습된 통계적 조직 확률 맵으로부터 사전 확률을 계산하고 베이지안 추론을 통해 유도된 레벨 셋에 결합하여 입력 영상의 유방 밀도를 측정한다.

결과: 통계적 조직 확률 모델의 학습에 사용되지 않은 100 장의 유방 X 선 영상의 밀도를 세 명의 유방 X 선 영상 전문가가 반자동 소프트웨어를 이용하여 측정하고 그 결과와 본 연구에서 제안한 자동 측정 방법의 결과의 상관계수는 0.93 이었으며, 이는 사전 통계 정보를 사용

하지 않은 레벨셋 방법의 상관계수인 0.47 과 비교하였을 때 본 연구에서 제안한 사전 통계 정보가 유방 밀도 측정에 효과적이라는 것을 입증한다.

결론: 본 연구에서 제안한 통계적 조직 확률 모델 기반의 레벨셋 방법은 전문가의 지식을 활용하는 직관적이면서도 효과적인 유방 밀도 자동 측정으로서 정량적인 밀도 수치와 측정 결과 영상을 동시에 출력함으로써 유방암 스크리닝을 통한 조기 유방암 검진에 크게 기여할 수 있을 것이다.

주요어 : 사전 통계, 레벨 셋, 유방 밀도, 정량적 측정, 디지털 유방 X 선 영상

학 번 : 2010-30598